University of Groningen

Oscillating features in the electromagnetic structure of the neutron

BESIII Collaboration; Ablikim, M.; Achasov, M.N.; Adlarson, P.; Ahmed, S.; Albrecht, M.; Aliberti, R.; Amoroso, A.; Kalantar-Nayestanaki, Nasser; Kappert, Rosa

IMPORTANT NOTE: You are advised to consult the publisher's version (publisher's PDF) if you wish to cite from it. Please check the document version below.

Document Version
Publisher's PDF, also known as Version of record

[Link to publication in University of Groningen/UMCG research database](#)

Citation for published version (APA):
BESIII Collaboration, Ablikim, M., Achasov, M. N., Adlarson, P., Ahmed, S., Albrecht, M., Aliberti, R., Amoroso, A., Kalantar-Nayestanaki, N., Kappert, R., Kavatsyuk, M., Messchendorp, J., & Rodin, V. (2021). Oscillating features in the electromagnetic structure of the neutron. *Nature Physics*, *17*(11), 1200-1204. https://doi.org/10.1038/s41567-021-01345-6

OPEN
Oscillating features in the electromagnetic structure of the neutron

The BESIII Collaboration*

The complicated structure of the neutron cannot be calculated using first-principles calculations due to the large colour charge of quarks and the self-interaction of gluons. Its simplest structure observables are the electromagnetic form factors[1], which probe our understanding of the strong interaction. Until now, a small amount of data has been available for the determination of the neutron structure from the time-like kinematical range. Here we present measurements of the Born cross section of electron–positron annihilation reactions into a neutron and anti-neutron pair, and determine the neutron's effective form factor. The data were recorded with the BESIII experiment at centre-of-mass energies between 2.00 and 3.08 GeV using an integrated luminosity of 647.9 pb^{-1}. Our results improve the statistics on the neutron form factor by more than a factor of 60 over previous measurements, demonstrating that the neutron form factor data from annihilation in the time-like regime is on par with that from electron scattering experiments. The effective form factor of the neutron shows a periodic behaviour, similar to earlier observations of the proton form factor. Future works—both theoretical and experimental—will help illuminate the origin of this oscillation of the electromagnetic structure observables of the nucleon.

The neutron is a bound system of three valence quarks and a neutral sea consisting of gluons and quark–anti-quark pairs. Although the proton was discovered in 1919 and the neutron in 1932, the structure of the nucleon is still not fully understood. Over the years, investigations of the nucleon have raised new questions in experiments and theory, such as the spin crisis[2] and mass decomposition[3]. One famous example in scattering experiments is the proton radius puzzle, showing a discrepancy of 2.7σ (where σ is significance) between measurements with muonic and electronic hydrogen[4–6], with some remaining mysteries still to be clarified by future experiments. Another controversy surrounds the remarkably different charge density of the neutron in various theoretical models, revealing an opposite sign of the mean square of the charge radius[7,8]. In annihilation experiments, there is a long-standing puzzle involving the results from electron–positron annihilation reported by the DM2 (ref. [9]) and FENICE[10] experiments, which seem to indicate that the photon–neutron interaction is stronger than the corresponding photon–proton interaction—an observation that is difficult to reconcile with theoretical expectations[11,12]. A recent example is an interesting oscillating behaviour observed in the proton form factor in a measurement by the BaBar experiment[13], indicating a complex structure in the effective form factor data. These open questions might be answered through measurements of observables such as the Born cross section $\sigma_B(q^2) \equiv \sigma_B$, the corresponding effective form factor $|G(q^2)| \equiv |G|$, as well as the electric $G_E(q^2) \equiv G_E$ and magnetic $G_M(q^2) \equiv G_M$ form factors of the nucleon (where q is the four momentum transfer carried by the virtual photon of the reac-

tion). All these form factors are functions of the squared momentum transfer, $q^2 = (k_1 + k_2)^2 = (p_1 + p_2)^2 = s$, where k_1, k_2, p_1 and p_2 are the incoming and outgoing four-momenta of the (anti-)lepton and (anti-)nucleon, respectively. The form factors parameterize the coupling of a virtual photon $\gamma^*(q^2)$ with the hadronic current J_{had}^μ. For electron–positron annihilation into a nucleon–anti-nucleon pair process, for which the leading-order Feynman diagram is shown in Fig. 1a, σ_B and $|G|$ are defined as

$$
\sigma_B = \frac{4\pi\alpha_{em}^2 \beta C(q^2)}{3q^2} \left[|G_M(q^2)|^2 + |G_E(q^2)|^2 \frac{1}{2\tau} \right],
$$
$$
|G| = \sqrt{\frac{2\tau |G_M(q^2)|^2 + |G_E(q^2)|^2}{2\tau + 1}}.
$$
(1)

Here α_{em} is the electromagnetic fine-structure constant, β is the centre-of-mass (c.m.) system velocity of the final-state nucleon or anti-nucleon, $\tau = q^2/4m_N^2$, m_N is the nucleon mass and $C(q^2)$ is the S-wave Sommerfeld–Gamow factor for the Coulomb correction[14], which is equal to 1 for neutral baryons.

The Beijing Electron–Positron Collider II is a symmetric electron–positron collider, operating in the c.m. energy ($\sqrt{s}$) region between 2.00 and 4.94 GeV. We study neutron and anti-neutron pairs produced in e^+e^- annihilations for $\sqrt{s}$ between 2.00 and 3.08 GeV. This dataset represents the first high-luminosity off-resonance energy scan, and enabled us to perform a precise measurement of σ_B and $|G|$ for the process $e^+e^- \to n\bar{n}$ at 18 c.m. energies. The Beijing Spectrometer III (BESIII) experiment[15] is optimized for the reconstruction of charged particles and photons using the main drift chamber (MDC) inner tracker to measure momenta and an electromagnetic calorimeter (EMC) constructed with CsI(Tl) crystals to measure energy deposition. A time-of-flight (TOF) system consisting of plastic scintillator bars between the MDC and EMC measures the flight time of charged particles. A method for the flight-time measurements for neutral particles that was specifically developed for this analysis is described in Methods. A muon counter (MUC) system is used to identify muons and to reject the cosmic ray background. The analysis of $e^+e^- \to n\bar{n}$ with the BESIII detector is very challenging due to the required reconstruction of the two neutral hadrons in the final state in the absence of a hadronic calorimeter and the need for a corresponding efficiency evaluation. A schematic of the BESIII detector with a typical response from the signal process $e^+e^- \to n\bar{n}$ is shown in Fig. 1b.

To maximize the reconstruction efficiency, the data are classified into three subsets ($i = A$, B and C) depending on the interactions of the signal particles within the detector. Events with signals from a knockoff proton interaction in the TOF plastic scintillators and the associated hadronic showers registered in the EMC from both neutron and anti-neutron are classified as category A. Category B comprises events with showers in the EMC from both particles, but only

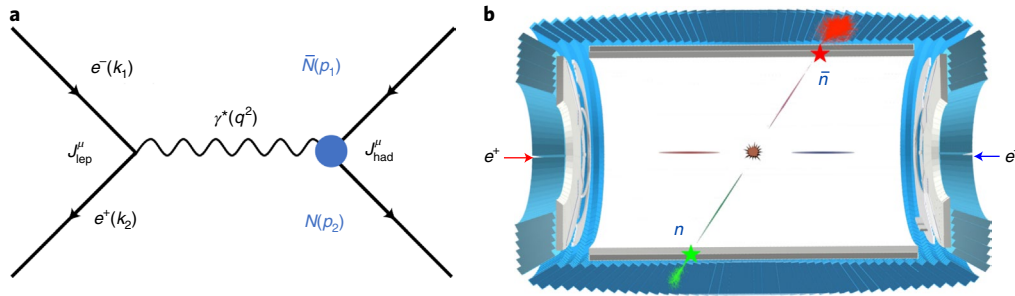*A list of authors and their affiliations appears online only.

Fig. 1 | Signal-process reaction and schematic of the response within the BESIII detector. a, The lowest-order Feynman diagram for the process $e^+e^- \rightarrow N\bar{N}$. Here k_1, k_2, p_1 and p_2 are the incoming and outgoing four-momenta of the (anti-)lepton and (anti-)nucleon, respectively; J^μ_{lep} and J^μ_{had} are the leptonic and hadronic vector currents, respectively; and $\gamma^\star(q^2)$ represents the virtual photon transferring the four-momentum $q^2 = -Q^2$ of the reaction. The blue blob represents the complex nucleon structure encoded by the electromagnetic form factors. **b,** Typical response in the BESIII detector for the signal process $e^+e^- \rightarrow n\bar{n}$ shown in a plane parallel to the electron–positron beam direction. The red (green) stars and showers represent the detector response of the signal process in the TOF system and EMC for the anti-neutron (neutron).

a knockoff proton interaction from the anti-neutron is measured. Events lacking any TOF interaction but with reconstructed hadronic showers measured in the EMC from both signal particles are classified as category C. Every signal event belongs to only one category, and the inclusion of all the three categories provides high efficiency for signal reconstruction. We combine the statistically independent results from the three categories using an inverse-variance weighting technique. More details on the signal reconstruction procedures are provided in Methods.

The data that pass the signal selection still contain non-negligible background contributions mostly coming from multi-hadronic processes, beam-associated processes and cosmic rays, as shown in Supplementary Fig. 2. We investigate the amount and distributions of the remaining background events with dedicated Monte Carlo (MC)-simulated events that mimic the detector response for various electrodynamic (that is, di-gamma) and multi-hadronic processes. The cosmic ray background and beam-associated backgrounds, including interactions between the beam and beam pipe, beam and residual gas, and Touschek effect[16], are studied with two data samples collected when the electron and positron beams were not in the collision mode. The number of genuine signal events $\mathcal{N}^s_i$ is extracted from the data samples by fitting to the following distributions: for the signal events in category A, we use the difference ΔT_n between the TOF of the neutron measured with the TOF system and the calculated expected flight time; for signal events in categories B and C, the fit is applied to the opening angle $\sphericalangle^n_{\bar{n}}$ between the measured positions of the neutron and anti-neutron assuming that they originated from the e^+e^- collision point. An unbinned maximum-likelihood fit is performed to determine $\mathcal{N}^s_i$. The likelihood function $\mathcal{F}_i$ is constructed by a set of probability density functions (PDFs) for the signal (PDF^s_i) and background (PDF^b_i) contributions and characterized by either ΔT_n or $\sphericalangle^n_{\bar{n}}$. To model the signal-event distribution PDF^s_i, we use the MC-simulated samples of the signal-event process generated with CONEXC[17]. Specifically,

$$\mathcal{F}_i\left[\Delta T_n(i=\text{A}), \sphericalangle^n_{\bar{n}}(i=\text{B, C})\right] = \mathcal{N}^s_i\text{PDF}^s_i + \sum_b \mathcal{N}^b_i\text{PDF}^b_i, \quad (2)$$

$(i = \text{A, B, C})$, $(b = \text{beam-associated, multi-hadronic, di-gamma})$.

The reconstruction efficiency, ε_i, for the signal process is determined from the exclusive signal MC simulation as well as from the data and additional MC simulations for the following physics processes: $e^+e^- \rightarrow J/\psi \rightarrow p\bar{n}\pi^-$, $e^+e^- \rightarrow J/\psi \rightarrow \bar{p}n\pi^+$, $e^+e^- \rightarrow p\bar{p}$ and $e^+e^- \rightarrow \gamma\gamma$. Using these samples, we correct the differences in the detector response between the data and signal MC simulation.

Details for the correction of the signal reconstruction efficiency are provided in Methods. The Born cross section, σ^i_B, and the corresponding form factor, $|G^i|$, are determined for each classification category from the following relationship.

$$\sigma^i_B = \frac{\mathcal{N}^s_i}{\mathcal{L}_{\text{int}}\varepsilon_i(1+\delta)}, |G^i| = \sqrt{\frac{\sigma^i_B}{\frac{4\pi\alpha^2_{\text{em}}\beta}{3q^2}\left(1+\frac{1}{2\tau}\right)}} \quad (3)$$

Here $\mathcal{L}_{\text{int}}$ is the measured integrated luminosity[18,19] and $(1+\delta)$ is the product of the initial-state radiation and vacuum polarization correction.

The results from categories A, B and C are consistent with each other within one standard deviation at all c.m. energies, as shown in Supplementary Fig. 4. We use a generalized least-squares method to combine these individual results to reduce the statistical uncertainty using the following expressions, where Δ indicates the uncertainty of a quantity and ρ indicates the correlation matrix of the three results.

$$\sigma_B = \sum_i w_i\sigma^i_B, \ \Delta\sigma_B = \sqrt{\frac{1}{\sum_i\sum_j W_{i,j}}}, \ w_i = \frac{\sum_j W_{i,j}}{\sum_i\sum_j W_{i,j}},$$

$$W = \left[\Delta\sigma^T\rho\Delta\sigma\right]^{-1}, (i = \text{A, B, C}) \quad (4)$$

The extracted results at 18 c.m. energies are listed in Table 1 and shown in Fig. 2. As sources of systematic uncertainty, we consider category-specific sources, as well as those that are common to two or more categories that introduce correlations. More details on signal extraction and the evaluation of systematic uncertainty sources are provided in Methods.

Our results for σ_B and $|G|$ substantially improve the overall precision of the available data for the neutron. For $\sqrt{s} = 2.0$, 2.1 and 2.4 GeV, the precision is improved over previous measurements from the FENICE and DM2 experiments by factors of about three, two and six, respectively. They reach a comparable precision to those from the SND experiment below $\sqrt{s} = 2.0$ GeV.

Our measurements are systematically below all other previously measured values above 2 GeV, while still in agreement within two standard deviations taking into account individual uncertainties. The FENICE experiment published results on the Born cross section for the $e^+e^- \rightarrow n\bar{n}$ and $e^+e^- \rightarrow p\bar{p}$ processes, reporting a ratio of $R_{np} = \sigma^{n\bar{n}}_B/\sigma^{p\bar{p}}_B = 1.69 \pm 0.49 > 1.00$ (ref. [10]), which corresponds to a stronger coupling of the virtual photon $\gamma^\star(q^2)$ with the neutron than with the proton. With the results from this analysis and a recent publication by the BESIII experiment on the Born cross section of $e^+e^- \rightarrow p\bar{p}$ (refs. [20,21]) that was extracted from the same data

Table 1 | Summary of results for the Born cross section σ_B and effective form factor $|G|$

$\sqrt{s}$ (GeV)	$\mathcal{L}_{int}$ (pb^{-1})	σ_B (pb)	$\lvert G \rvert$ ($\times 10^{-2}$)	$\sqrt{s}$ (GeV)	$\mathcal{L}_{int}$ (pb^{-1})	σ_B (pb)	$\lvert G \rvert$ ($\times 10^{-2}$)
2.0000	10.10	$386 \pm 55 \pm 37$	$19.0 \pm 1.3 \pm 0.9$	2.3864	22.5	$87.0 \pm 8.0 \pm 6.0$	$8.4 \pm 0.4 \pm 0.3$
2.0500	3.34	$256 \pm 67 \pm 16$	$14.8 \pm 1.9 \pm 0.5$	2.3960	66.9	$98.0 \pm 5.0 \pm 6.0$	$8.9 \pm 0.2 \pm 0.3$
2.1000	12.20	$207 \pm 24 \pm 19$	$13.0 \pm 0.8 \pm 0.6$	2.6454	67.7	$22.0 \pm 2.0 \pm 2.0$	$4.5 \pm 0.2 \pm 0.2$
2.1250	108.00	$145 \pm 6 \pm 12$	$10.8 \pm 0.2 \pm 0.4$	2.9000	105.0	$8.5 \pm 1.1 \pm 0.7$	$3.0 \pm 0.2 \pm 0.1$
2.1500	2.84	$149 \pm 38 \pm 12$	$10.9 \pm 1.4 \pm 0.4$	2.9500	15.9	$7.7 \pm 2.9 \pm 1.0$	$2.9 \pm 0.5 \pm 0.2$
2.1750	10.60	$99 \pm 16 \pm 8$	$8.8 \pm 0.7 \pm 0.4$	2.9810	16.1	$8.6 \pm 2.9 \pm 1.0$	$3.1 \pm 0.5 \pm 0.2$
2.2000	13.70	$83 \pm 12 \pm 6$	$8.1 \pm 0.6 \pm 0.3$	3.0000	15.9	$8.6 \pm 3.4 \pm 1.4$	$3.1 \pm 0.6 \pm 0.2$
2.2324	11.90	$88 \pm 13 \pm 7$	$8.3 \pm 0.6 \pm 0.3$	3.0200	17.3	$8.0 \pm 2.8 \pm 1.0$	$3.0 \pm 0.5 \pm 0.2$
2.3094	21.10	$93 \pm 9 \pm 7$	$8.6 \pm 0.4 \pm 0.3$	3.0800	126.0	$3.9 \pm 0.7 \pm 0.5$	$2.1 \pm 0.2 \pm 0.1$

The first error is statistical and the second one, systematic. Here $\sqrt{s}$ represents the c.m. energy and $\mathcal{L}_{int}$, the integrated luminosity.
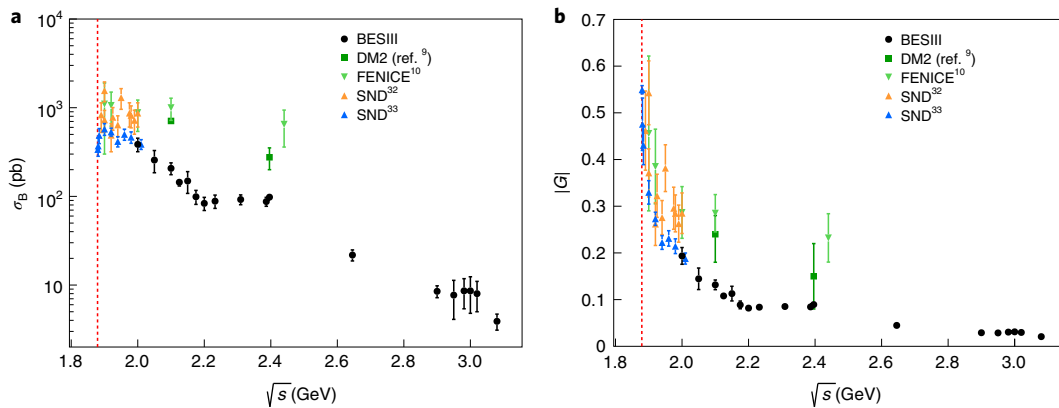

Fig. 2 | Results for the Born cross section σ_B and corresponding form factor $|G|$ of the neutron. a,b, Born cross section σ_B (**a**) and effective form factor $|G|$ (**b**) with respect to the c.m. energy. The black solid circles are the BESIII results from this analysis. Existing results from DM2 (ref. [9]), FENICE[10], and two SND[32,33] experiments are shown as green squares, green downward triangles, and orange and blue upward triangles, respectively. The red dashed line indicates the production threshold for the signal process. For all the data points, the total uncertainty (quadratic sum of statistical and systematic errors, corresponding to a 68.3% confidence level of a normal distribution) is plotted.

samples, we test the ratio of the cross sections, as shown in Fig. 3a. It is found that R_{np} is smaller than 1 at all energies, in contrast to the results obtained by the FENICE experiment. Our result shows that the photon–proton interaction is stronger than the corresponding photon–neutron interaction, as expected by most theoretical predictions, and clarifies the photon–nucleon interaction puzzle that has persisted for over 20 years.

The values for $|G|$ obtained in this analysis are used to search for a neutron counterpart to the oscillatory behaviour that was observed for protons[13]. In fact, as shown in Fig. 3b, after subtracting the well-established dipole formula $G_D(q^2) \equiv G_D$, that is,

$$G_{osc}(q^2) = |G| - G_D, \quad G_D(q^2) = \frac{\mathcal{A}_n}{\left(1 - \frac{q^2}{0.71\ (\text{GeV}^2)}\right)^2}, \quad (5)$$

where $\mathcal{A}_n = 3.5 \pm 0.1$ is a normalization factor; the data exhibit a similar behaviour. The $G_{osc}(q^2) \equiv G_{osc}$ values for both neutron and proton can be simultaneously fitted by the function F_{osc} of the relative momentum p (proposed in ref. [22]) with a common momentum frequency C.

$$F_{osc}^{n,p} = A^{n,p} \exp\left(-B^{n,p} p\right) \cos\left(Cp + D^{n,p}\right), \quad p \equiv \sqrt{E^2 - m_{n,p}^2}, \quad (6)$$

$$E \equiv \frac{q^2}{2m_{n,p}} - m_{n,p}$$

Here A is the normalization; B, the inverse oscillation damping; and D, the phase. The fit yields $C = (5.55 \pm 0.28)\ \text{GeV}^{-1}$ and a phase difference of $\Delta D = |D_p - D_n| = (125 \pm 12)°$ with a goodness of fit $\chi^2/\text{dof} = 50/47$ and a statistical significance of over 5σ with respect to a null oscillation hypothesis, where dof is degrees of freedom, and D_p and D_n are the phase parameters from simultaneous fit for the proton and neutron, respectively. The periodic structure of $|G|$ for the proton demonstrates a deviation from a modified dipole behaviour. We observe a corresponding behaviour with a similar frequency for the neutron, but with a large phase difference. The results imply that there are some not yet understood intrinsic dynamics that are responsible for almost orthogonal oscillations. Possible explanations for this oscillation are interference effects from final-state re-scattering[23] or the influence of a resonant structure[24]. Theoretical investigations as well as more experimental data might help illuminate the origin of this oscillation of the electromagnetic structure observables of the nucleon.

The results provide an enhanced insight into the fundamental properties of the neutron. The results can be used to constrain parameterizations of the generalized part in the distribution that are closely related to the neutron spin[25] and are related to the neutron mass according to the Feynman–Hellmann theorem[26]. Furthermore, the extracted form factors can be directly translated into the neutron radius in the Breit frame[27], and—when combined with lepton scattering results—provide a useful input to the controversy
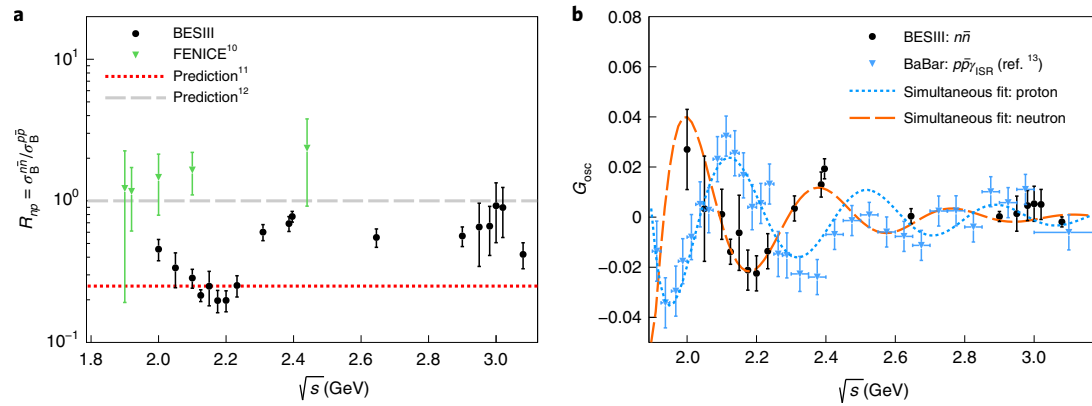
Fig. 3 | Results for the R_{np} ratio and form factor $|G|$ deviation from the dipole law with respect to $\sqrt{s}$. a, The R_{np} ratio is shown using the results from this analysis and the existing data of the proton[20] (black circles) together with the results from the FENICE experiment[10] (green downward triangles). The red fine-dashed and grey wide-dashed lines are two predictions from ref. [11] and ref. [12], respectively. **b**, Fit to the deviation of the effective form factor $|G|$ of the nucleon from the dipole law. The black circles show the results from this work, while the blue downward triangles indicate the results for the proton from the BaBar experiment[13]. The orange wide-dashed and blue fine-dashed lines are the fit results with a common momentum frequency C to the neutron and proton data obtained using equation (6), respectively. For all the data points, the total uncertainty (quadratic sum of statistical and systematic errors, corresponding to a 68.3% confidence level of a normal distribution) is plotted.

surrounding the neutron charge radius[7,8]. A detailed knowledge of the electromagnetic structure of the neutron is needed for the understanding of many fundamental processes. For example, the distribution of neutrons in nuclei and their internal structure plays a major role in the calculations of neutron-star radii[28]. A possible quantum chromodynamics phase transition from nuclear matter to quark–gluon plasma involves the neutron structure, and annihilation reactions play a major role in the simulation of measurements[29,30]. The observation of the light curve and gravitational-wave signals of a nearby neutron-star merger (as observed recently by gravitational-wave detectors) allows the identification of different contributions to this violent process in terms of nuclear physics, nucleon structure and general relativity[31].

Online content

Any methods, additional references, Nature Research reporting summaries, source data, extended data, supplementary information, acknowledgements, peer review information; details of author contributions and competing interests; and statements of data and code availability are available at https://doi.org/10.1038/s41567-021-01345-6.

References

1. Lomon, E. L. & Pacetti, S. Timelike and spacelike electromagnetic form factors of nucleons, a unified description. *Phys. Rev. D* **85**, 113004 (2012); erratum **86**, 039901 (2012).
2. Ashman, J. et al. A measurement of the spin asymmetry and determination of the structure function g_1 in deep inelastic muon-proton scattering. *Phys. Lett. B* **206**, 364–370 (1988).
3. Ji, X. D. A QCD analysis of the mass structure of the nucleon. *Phys. Rev. Lett.* **74**, 1071–1074 (1995).
4. Bernauer, J. C. et al. High-precision determination of the electric and magnetic form factors of the proton. *Phys. Rev. Lett.* **105**, 242001 (2010).
5. Pohl, R. et al. The size of the proton. *Nature* **466**, 213–216 (2010).
6. Xiong, W. et al. A small proton charge radius from an electron–proton scattering experiment. *Nature* **575**, 147–150 (2019).
7. Miller, G. A. Charge density of the neutron and proton. *Phys. Rev. Lett.* **99**, 112001 (2007).
8. Shintani, E., Ishikawa, K. I., Kuramashi, Y., Sasaki, S. & Yamazaki, T. Nucleon form factors and root-mean-square radii on a (10.8 fm)^4 lattice at the physical point. *Phys. Rev. D* **99**, 014510 (2019); erratum **102**, 019902 (2020).
9. Biagini, M. E., Cugusi, L. & Pasqualucci, E. *U*-spin considerations to guess the unknown time-like neutron form factors. *Z. Phys. C* **52**, 631–634 (1991).
10. Antonelli, A. The first measurement of the neutron electromagnetic form factors in the timelike region. *Nucl. Phys. B* **517**, 3–35 (1998).
11. Chernyak, V. L. & Zhitnitsky, A. R. Asymptotic behavior of exclusive processes in QCD. *Phys. Rep.* **112**, 173–318 (1984).
12. Pacetti, S., Baldini, R. F. & Tomasi-Gustafsson, E. Proton electromagnetic form factors: basic notions, present achievements and future perspectives. *Phys. Rep.* **550–551**, 1–103 (2015).
13. Lees, J. P. Study of $e^+e^- \to p\bar{p}$ via initial-state radiation at BABAR. *Phys. Rev. D* **87**, 092005 (2013).
14. Arbuzov, A. B. & Kopylova, T. V. On relativization of the Sommerfeld-Gamow-Sakharov factor. *J. High Energ. Phys.* **2012**, 9 (2012).
15. Ablikim, M. et al. Design and construction of the BESIII detector. *Nucl. Instrum. Meth. A* **614**, 345–399 (2010).
16. Bernardini, C. et al. Lifetime and beam size in a storage ring. *Phys. Rev. Lett.* **10**, 407–409 (1963).
17. Ping, R. G. An exclusive event generator for e^+e^- scan experiments. *Chinese Phys. C* **38**, 083001 (2014).
18. Ablikim, M. et al. Luminosity measurements for the R scan experiment at BESIII. *Chinese Phys. C* **41**, 063001 (2017).
19. Ablikim, M. et al. Measurement of integrated luminosity and center-of-mass energy of data taken by BESIII at $\sqrt{s} = 2.125$ GeV. *Chinese Phys. C* **41**, 113001 (2017).
20. Ablikim, M. et al. Measurement of proton electromagnetic form factors in $e^+e^- \to p\bar{p}$ in the energy region 2.00–3.08 GeV. *Phys. Rev. Lett.* **124**, 042001 (2020).
21. Ablikim, M. et al. Study of the process $e^+e^- \to p\bar{p}$ via initial state radiation at BESIII. *Phys. Rev. D* **99**, 092002 (2019).
22. Bianconi, A. & Tomasi-Gustafsson, E. Periodic interference structures in the timelike proton form factor. *Phys. Rev. Lett.* **114**, 232301 (2015).
23. Bianconi, A. & Tomasi-Gustafsson, E. Phenomenological analysis of near-threshold periodic modulations of the proton timelike form factor. *Phys. Rev. C* **93**, 035201 (2016).
24. Lorenz, I. T., Hammer, F. W. & Meißner, U. G. New structures in the proton-antiproton system. *Phys. Rev. D* **92**, 034018 (2015).
25. Thomas, A. W. Interplay of spin and orbital angular momentum in the proton. *Phys. Rev. Lett.* **101**, 102003 (2008).
26. Pagels, H. Departures from chiral symmetry: a review. *Phys. Rep.* **16**, 219–311 (1975).
27. Hand, L. N., Miller, D. G. & Wilson, R. Electric and magnetic form factors of the nucleon. *Rev. Mod. Phys.* **35**, 335–349 (1963).
28. Hagen, G. et al. Neutron and weak-charge distributions of the ^{48}Ca nucleus. *Nat. Phys.* **12**, 186–190 (2015).
29. Andronic, A., Braun-Munzinger, P., Redlich, K. & Stachel, J. Decoding the phase structure of QCD via particle production at high energy. *Nature* **561**, 321–330 (2018).
30. Adamczewski-Musch, J. et al. Probing dense baryon-rich matter with virtual photons. *Nat. Phys.* **15**, 1040–1045 (2019).

31. Bauswein, A. Equation of state constraints from multi-messenger observations of neutron star mergers. *Ann. Phys.* **411**, 167958 (2019).
32. Achasov, M. N. et al. Study of the process $e^+e^- \to n\bar{n}$ at the VEPP-2000 e^+e^- collider with the SND detector. *Phys. Rev. D* **90**, 112007 (2014).
33. Druzhinin, V. P. & Serednyakov, S. I. Measurement of the $e^+e^- \to n\bar{n}$ cross section with the SND detector at the VEPP-2000 collider. *EPJ Web Conf.* **212**, 07007 (2019).

Publisher's note Springer Nature remains neutral with regard to jurisdictional claims in published maps and institutional affiliations.

Methods

MC simulations used in this analysis. Signal MC samples have been produced for the optimization of signal selection, determination of signal efficiency and estimation of corrections from the quantum electrodynamics initial-state radiation (ISR) events. The signal MC sample is produced with the CONEXC generator[17], which is designed to simulate events up to the next-to-leading order and using the implementation of vacuum polarization by Jegerlehner[34]. Since the $n\bar{n}$ final state is electrically neutral, no QED final-state radiation effects occur. Background from multi-hadronic processes is estimated from MC simulations generated with LUND[35]. Cross sections and angular distributions from measured processes are implemented in the generator, while unmeasured processes are generated as phase space. Background from QED processes, such as $e^+e^- \to e^+e^-$ or $e^+e^- \to \gamma\gamma$ are generated with BABAYAGA[36] in the next-to-next-to-leading order including vacuum polarization, ISR and final-state radiation effects. Finally, we use MC simulation for the control channels $e^+e^- \to J/\Psi \to p\bar{n}\pi^- (\bar{p}n\pi^+)$, which are generated with KKMC[37]. All the MC simulations are generated according to the integrated luminosity of the collider data, containing equal or larger numbers of events than those available from the data.

TOF-based algorithm for reconstruction of neutral particles. A common method in signal classification categories A and B, which combines the response from the EMC and TOF, is described as follows. The most energetic shower in an event is identified as the anti-neutron $\bar{n}$. Its position vector in the EMC response $\mathbf{V_{EMC1}}$ with respect to the e^+e^- interaction point (IP) $\mathbf{V_{IP}}$ is associated with the closest TOF response with position vector $\mathbf{V_{TOF1}}$, if the distance in the TOF plane $\Delta^{EMC1}_{TOF1} = |\mathbf{V_{EMC1}} - \mathbf{V_{TOF1}}|$ is smaller than the azimuthal span of three TOF counters. The flight length of the anti-neutron to the TOF response is $L_{\bar{n}} = |\mathbf{V_{TOF1}} - \mathbf{V_{IP}}|$. The flight time of the anti-neutron T_{TOF1} is determined by an algorithm[38] using the hypothesis of a photon producing the TOF response. The expected flight time for a photon from the IP to the TOF response $\mathbf{V_{TOF1}}$ is $T^{exp}_{\gamma} = L_{\bar{n}}/c$, where c is the speed of light in a vacuum. For the time difference $\Delta T_{\bar{n}} = T_{TOF1} - T^{exp}_{\gamma}$, values different from zero are expected for the anti-neutron; therefore, this criterion can be used for discriminating the photon background. A similar approach is chosen for the reconstruction of the neutron candidate n. The time difference $\Delta T_n = T^{obs}_n - T^{exp}_n$ is used to identify n candidates. Further, T^{obs}_n is the measured time and $T^{exp}_n = L_n/(\beta c)$ is the expected flight time under the hypothesis of a neutron, where L_n is the flight length of the neutron to the coordinates of the TOF response. Furthermore, the opening angle between the anti-neutron position vector $\mathbf{V_{EMC1}}$ and the measured TOF position vector $\mathbf{V_{TOF2'}}$ can be used to suppress events with more than two final-state particles and beam-associated background. The process of $e^+e^- \to J/\psi \to \pi^+\pi^-\pi^0$ is used to verify the photon detection efficiency with the above method. Supplementary Fig. 5 shows that the data are in excellent agreement with the MC simulation (difference of <1%). Additionally, we verify the efficiency of the neutral TOF reconstruction with the well-known channel $e^+e^- \to \gamma\gamma$, as well as with $e^+e^- \to J/\Psi \to n\bar{n}$. The results for the cross section and branching fraction are in excellent agreement with the world reference, as shown in Supplementary Tables 4 and 5, respectively.

Cosmic ray background rejection with MUC. We use the MUC system to reject the cosmic ray background in categories B and C. With nine layers of resistive plates (in the barrel region) with iron absorbers between them, the developed algorithm is capable of distinguishing between the impact from particles coming from the IP of the BESIII detector and the response from the cosmic ray particles entering the detector from the outside. We evaluate the available information from the MUC and apply a criterion on the last layer with a hit response. A detailed validation of the efficiency for this method has been performed by studying the MUC response for neutrons, anti-neutrons and photons from the dedicated MC samples and collision data. The detector response from the cosmic ray background is studied from the non-collision data samples at $\sqrt{s} = 2.2324\,GeV$ and $\sqrt{s} = 2.6444\,GeV$ and is stable over the analysed energy range. The data and MC simulation are in agreement, as shown in an example with the collision data, non-collision data and MC simulation for dedicated signal and background processes in Supplementary Fig. 6 for signal samples of category C at $\sqrt{s} = 2.396\,GeV$.

General signal-event reconstruction criteria. Signal events must contain no charged tracks and one or two reconstructed showers in the EMC as neutron n and anti-neutron $\bar{n}$ candidates. The most energetic shower $(\bar{n})$ must be within $|\cos\theta| < 0.8$ and have an energy deposition in the range between 0.5 and 2.0 GeV.

Signal classification category A. Signal events must satisfy the following requirements for anti-neutron selection: the number of hits in the EMC in a 50° cone around the anti-neutron shower (N^{50}_{hits}) must be within the window of $30 < N^{50}_{hits} < 140$. Hits in the EMC are defined as signal responses from particle showers. The reconstructed position of an EMC hit is the centre of gravity from the shower. The most energetic shower must be within $|\cos\theta| < 0.7$ to ensure an efficient rejection of the $e^+e^- \to \gamma\gamma$ process. To select the neutron shower, a cut on $|\Delta T_n| < 4\,ns$ is applied. If a second EMC shower is found, a requirement of $0.06 < E_n < 0.70\,GeV$ on the deposited energy is applied at $\sqrt{s} \geq 2.6444\,GeV$. The

different energy cuts are performed because high-momentum neutrons easily penetrate into the EMC, and therefore, an extra energy cut is applied to improve the signal-to-background ratio without reducing the signal efficiency. To further suppress physics and beam-associated background, we anticipate the back-to-back kinematics of the signal process. We require the opening angles between $\mathbf{V_{EMC1}}$ and $\mathbf{V_{TOF2'}}$ and between $\mathbf{V_{EMC1}}$ and $\mathbf{V_{EMC2}}$ to be larger than 3 rad. The flight-time difference between the two final-state particles $\Delta T_{n\bar{n}} = |T_{TOF1} - T_{TOF2}|$ is required to be smaller than 4 ns.

Signal classification category B. For the anti-neutron, $|\Delta T_{\bar{n}}| > 0.5\,ns$ is required. The neutron energy deposition in the EMC must be within $0.06 < E_n < 0.60\,GeV$. Both particles must be reconstructed within $|\cos\theta| < 0.75$. No signal in the MUC from the last three layers is allowed, which ensures good rejection power against the cosmic ray background. Finally, a boosting decision tree (BDT) method is used to reduce the remaining background. The BDT uses multiple observables from the EMC and TOF systems with a discriminator requirement of >0.1 for signal-event reconstruction.

Signal classification category C. An anti-neutron is reconstructed when the EMC shower position requirement is $|\cos\theta| < 0.75$ and the second moment of the anti-neutron shower to follow $\sum E_i r_i^2/E_i > 20\,cm^2$, where E_i is the deposition energy in the ith crystal and r_i is the distance between the centre of the ith crystal and centre of gravity of the shower. The number of hits in the EMC within 50° around the $\bar{n}$ position is required to be $35 < N^{50}_{hits} < 100$. Neutron reconstruction is the same as for signal events classified under category B. To further suppress the remaining background, the same requirement as in category B is applied on the MUC, namely, the opening angle between the EMC showers from n and $\bar{n}$ must be larger than 150° and the total energy deposition E_{extra} outside the 50° cones around the neutron and anti-neutron shower position in the EMC must be smaller than 0.15 GeV.

Determination of number of signal events. To determine the number of reconstructed signal events $\mathcal{N}^s_i$, a composite model fit $\mathcal{F}_i$ is performed to the distribution of ΔT_n for category A events and to $\triangleleft^{\bar{n}}_n$ for category B and C events, as discussed in the main text. The background normalizations are determined using the luminosity of the data samples and the theoretical cross sections for the contributing processes. The normalization for the beam-associated background is obtained using the data-taking time of the non-collision and collision samples when applicable, or via curve fitting of the background event distribution. The fit optimization for each category is performed by minimizing the global negative log likelihood with the MIGRAD[39] package by means of a modified version of the David–Fletcher–Powell method[40] taking into account the 18 local negative log likelihoods from each dataset. The HESSE[39] algorithm calculates a full second-derivative matrix of the model parameter space to improve the uncertainty determination. The following MINOS error analysis is performed for a further optimization of the parameter error estimation. While the globally optimized solution may not be optimal at a specific $\sqrt{s}$, this approach improves the fit stability. The optimized fits for the three signal classification categories A, B and C are shown for the data at $\sqrt{s} = 2.3960\,GeV$ (Supplementary Fig. 2).

Reconstruction efficiency correction. The efficiency from signal MC simulation ε_{MC} is imperfect. The reason is the difficulty of simulating the response of hadronic showers in the detector material due to their complex structure and number of components. As a consequence, the distributions for observables based on the TOF or EMC detector response for MC simulation are not in agreement with the corresponding distributions from the collision data. This leads to an imprecise ε_{MC}, which needs to be corrected. In this analysis, we chose to correct the ε_{MC} with a data-driven method. The determination of the corrected reconstruction efficiency ε_{cor} is individually performed for each signal-event classification category $i = A$, B and C.

1. To study the efficiency corrections that only depend on either neutron or anti-neutron selection observables, the two control channels $e^+e^- \to J/\psi \to \bar{p}n\pi^+$ and $e^+e^- \to J/\psi \to p\bar{n}\pi^-$ are used. These control channels include two charged particles in the final state, which can be used to predict the position of the EMC shower from the neutron and anti-neutron, respectively. This allows us to precisely study the detector impact from a neutron and anti-neutron from the data and compare with the corresponding MC simulation. The selection of the control channels follows the discussion in ref. [41]. With the selection of control channels, a requirement on the recoil momentum $|\mathbf{p}^{recoil}_{p\pi^- (\bar{p}\pi^+)}| = |\mathbf{p}_{J/\psi} - \mathbf{p}_{p(\bar{p})} - \mathbf{p}_{\pi^- (\pi^+)}|$ is applied to restrict the momentum of the neutron (anti-neutron) from the control channel to the corresponding signal-process final-state particle momentum $|\mathbf{p}_{n(\bar{n})}| = \sqrt{(\sqrt{s}/2)^2 - m^2_{n(\bar{n})}}$. The reference sample for the process $J/\psi \to p\bar{n}\pi^- (J/\psi \to \bar{p}n\pi^+)$ contains a wide momentum range (50.0 MeV c^{-1} to 1.4 GeV c^{-1}) and almost 4π range of acceptance $(\cos\theta \in [-0.93, 0.93])$ for n $(\bar{n})$. The n $(\bar{n})$ momentum $|\vec{\mathbf{p}}|$ for both particles of the leading-order signal process $e^+e^- \to n\bar{n}$ is fixed because of two-particle kinematics, for example, at $\sqrt{s} = 2.125\,GeV$ to $|\vec{\mathbf{p}}|_{n(\bar{n})} = 0.5\,GeV\,c^{-1}$, within the coverage of the reference

sample. A deviation from the fixed momentum value occurs due to detector resolution as well as ISR events from the emission of low-energy photons. A sub-sample with a similar momentum $|\vec{p}|$ and at the same position in the EMC with respect to $\cos\theta$ (polar angle of n ($\bar{n}$)) as the signal-process particle is selected to reduce the difference in kinematics. The category-specific selection criteria for the neutron (anti-neutron) are applied for both, and the control-sample MC simulation and the data and corresponding selection efficiencies $\varepsilon_n^{\mathrm{data}}$, $\varepsilon_{\bar{n}}^{\mathrm{data}}$, $\varepsilon_n^{\mathrm{MC}}$ and $\varepsilon_{\bar{n}}^{\mathrm{MC}}$ are determined. The final efficiency correction $\mathcal{C}_{n\bar{n}}$ is determined as follows.

$$\mathcal{C}_{n\bar{n}} = \sum_{j,k} \mathcal{M}_{j,k} w_{j,k}, \; \Delta\mathcal{C}_{n(\bar{n})} = \sqrt{\sum_{j,k} (\Delta\mathcal{M}_{j,k})^2 w_{j,k}^2},$$

$$\mathcal{M}_{j,k} = \frac{\varepsilon_n^{\mathrm{data}}(\mathbf{p},\cos\theta)\varepsilon_n^{\mathrm{data}}(\mathbf{p},-\cos\theta)}{\varepsilon_n^{\mathrm{MC}}(\mathbf{p},\cos\theta)\varepsilon_n^{\mathrm{MC}}(\mathbf{p},-\cos\theta)} \tag{7}$$

Here $w_{j,k}(p,\cos\theta)$ is the normalized distribution in the momentum–position space from the signal MC simulation after all the selection criteria are applied. The negative sign of $\cos\theta$ for neutron efficiencies takes into account the back-to-back behaviour of the signal process. The absolute value is determined by using $\Delta\mathcal{M}_{j,k}$ as the individual error in the corresponding bin (j,k) from the correction matrix $\mathcal{M}$, and the signal distribution after all the selection criteria applied in the corresponding bin $w_{j,k}$.

2. For category C, the disagreement between the signal MC simulation and data for the selection criterion E_{extra} is studied with the process $e^+e^- \to p\bar{p}$. The process is selected as discussed in ref. [20]. To avoid biases, the selection criterion on $E/\mathbf{p}$ is replaced by the requirement on the proton EMC shower of $|\cos\theta| < 0.8$. The extra energy E_{extra} is defined as the energy deposition in the EMC not coming from n or $\bar{n}$. A cone is constructed around the flight direction of n ($\bar{n}$) with an opening angle of 20° (50°)°. The n and $\bar{n}$ energy deposition in the EMC comes from the hadronic showers of n and annihilation of $\bar{n}$. Both respective signals are very similar to the hadronic showers of p and annihilation of $\bar{p}$. The energy deposition due to the Bethe–Bloch energy loss can be neglected here. Radiative electromagnetic processes are absent at this $p/\bar{p}$ energy. E_{extra} contains all the energy deposition in the EMC, excluding all the energy deposited in the n ($\bar{n}$) cones. Since the control channel $e^+e^- \to p\bar{p}$ is a similar two-particle final state, one can define the cones for p and $\bar{p}$ in the same way as for $e^+e^- \to n\bar{n}$, and the E_{extra} distribution contains the same kind of EMC response (for example, from the machine background in the EMC; recoiled secondary particles from the $\bar{n}$ ($\bar{p}$) annihilation, which may be have a large angle with the $\bar{n}$ ($\bar{p}$) flight direction and are not included in the 50° cone; showers produced by cosmic rays; etc.). The reason why the channel $e^+e^- \to p\bar{p}$ is used for this study is the similarity between $\bar{n}$ and $\bar{p}$ annihilation. Using this hypothesis, we study the cut efficiency for E_{extra} from the clean selected sample of $e^+e^- \to p\bar{p}$ events from the data and from the signal MC simulation for $e^+e^- \to n\bar{n}$ and determine the efficiency correction $\mathcal{C}_{\mathrm{extra}} = \varepsilon_{\mathrm{extra}}^{p\bar{p},\mathrm{data}}/\varepsilon_{\mathrm{extra}}^{n\bar{n},\mathrm{MC}}$.

3. Determination of trigger efficiency:

   1. The average trigger efficiency, ϵ_{trg}, is defined as

$$\epsilon_{\mathrm{trg}} = \sum_{\mathrm{bin}} \rho(E)_{\mathrm{bin}} \mathrm{Trg}(E)_{\mathrm{bin}}, \; \mathrm{Trg}(E) = 0.5 + 0.5\mathrm{Erf}\left(\frac{E-a}{b}\right), \tag{8}$$

where $\rho(E)$ is the normalized, binned spectrum of the total energy deposition in the EMC from the signal process $e^+e^- \to n\bar{n}$. $\mathrm{Trg}(E)$—the probability that any event will be triggered under the total energy deposition E in the EMC—is obtained with an analysis of $e^+e^- \to p\bar{p}$. To prevent any bias in the EMC, no selection criteria from the EMC are used to select $e^+e^- \to p\bar{p}$, and trigger conditions from the MDC and TOF are pre-required to study the EMC response from the control channel. A conditional energy dependence of the EMC trigger is obtained by comparing the number of events passing the MDC+TOF+EMC trigger condition with the events that only pass the MDC+TOF trigger conditions (following the approach in ref. [42]):

$$P_{\mathrm{trigger}}(\mathrm{EMC}) = \frac{P_{\mathrm{trigger}}(\mathrm{EMC+MDC+TOF})}{P_{\mathrm{trigger}}(\mathrm{MDC+TOF})}, \tag{9}$$

$P_{\mathrm{trigger}}(\mathrm{MDC+TOF})$ is close to 1 (ref. [42]); therefore, it is assumed that $P_{\mathrm{trigger}}(\mathrm{EMC})$ is a reasonable evaluation of an independent trigger energy dependence. The obtained $P_{\mathrm{trigger}}(\mathrm{EMC})$ is fitted with the function $\mathrm{Trg}(E)$ (equation (8), right side). The parameters from the fit are determined to be $a = 0.758 \pm 0.005$ and $b = 0.334 \pm 0.009$.

   2. $\mathrm{Trg}(E)$ is not sensitive to the magnetic field, which is studied by the application of different selection conditions (this conclusion is drawn from the following facts: at BESIII, the magnetic field is 0.9 T and the inner EMC radius is 94 cm (table 17 in ref. [15]). As long as a charged proton/anti-proton carries a transverse momentum more than $p_T = 0.25\,\mathrm{GeV}\,c^{-1}$, it can reach the EMC. Thus, choosing $e^+e^- \to p\bar{p}$ events at $\sqrt{s}=2.125$, 2.396 and 2.665 GeV ($\sqrt{s}=2.125$; $p_T = 0.30\,\mathrm{GeV}\,c^{-1}$ at $\cos\theta=0.8$) is reasonable to determine the EMC trigger energy dependence $\mathrm{Trg}(E)$). As described

above, $\mathrm{Trg}(E)$ is tested with $e^+e^- \to p\bar{p}$ events from different $\sqrt{s}$ samples under different transverse momenta p_T of the proton, and it is found that $\mathrm{Trg}(E)$ is stable under different p_T values and the only difference is the statistical precision. The final $\mathrm{Trg}(E)$ is determined at high p_T.

3. The correct reconstruction of the total energy deposition in the EMC is crucial for the correct determination of the trigger efficiency. To obtain a reliable total energy deposition distribution $\rho(E)$ from the signal process, the control sample $J/\psi \to p\bar{n}\pi^-$ (+c.c. for the similar correction of the neutron impact in the EMC) is used to correct the energy deposition for the (anti-)neutron in the EMC from the signal MC simulation.

4. $\mathrm{Trg}(E)$ represents a probability that any event will be triggered under the total energy deposition E in the EMC, independent from the particle type of the process. Therefore, the obtained EMC trigger energy dependence $\mathrm{Trg}(E)$ is re-weighted with the corrected energy spectrum $\rho(E)$ from the signal process $e^+e^- \to n\bar{n}$. This approach is the best available way to reduce potential bias from the deflection of the magnetic field and a solution independent of the difference between anti-proton and anti-neutron annihilation in the detector material.

4. For categories B and C, corrections due to the selection criteria on the MUC have been studied in a similar way as for n- and $\bar{n}$-based selection criteria. They are found to be negligible, and possible residual effects are included in the systematic uncertainty.

The corrected reconstruction efficiency $\varepsilon_{\mathrm{cor}}$ is the product from the signal MC efficiency $\varepsilon_{\mathrm{MC}}$ and the above discussed contributions is as follows.

$$\varepsilon_{\mathrm{cor}} = \varepsilon_{\mathrm{MC}} \prod_i \mathcal{C}_i (i = n\bar{n}, \mathrm{MUC}, \mathrm{extra}, \mathrm{trg}) \tag{10}$$

Evaluation of systematic uncertainty. In the first step, the systematic uncertainty on the Born cross section and effective form factor are determined for each signal classification category. For the final results, the individual systematic uncertainties are combined. The following contributions are studied:

- The systematic uncertainty from the luminosity measurement δ_{L} is quoted from ref. [18].
- The selection criteria for the signal process $e^+e^- \to n\bar{n}$ have been corrected for the difference between the MC simulation and real data using a data-driven approach. We take one standard deviation of the combined efficiency corrections as the systematic uncertainty due to signal selection δ_{sel}^i.
- The uncertainty due to the fit procedure for the extraction of a signal event from the data combines the contributions from the fitting range, signal and background shape models. A sum in quadrature of these contributions represents the systematic uncertainty due to the fit δ_{fit}^i.
- The dependence of the angular distribution of the final-state particles can introduce a systematic effect on the reconstruction efficiency. To take this into account, we generate two extreme cases for the signal MC simulation samples according to the angular analysis results for R_{em}^i, taking into account the corresponding uncertainty. The difference between the reconstruction efficiency from the signal MC simulation with the nominal signal MC and the two extreme cases is taken as the systematic model uncertainty δ_{model}.
- The uncertainty from the trigger efficiency δ_{trg}^i is considered as the difference between the nominal results $\mathcal{C}_{\mathrm{trg}}^i$ with the results obtained using values from multi-hadronic final states for the parameters a and b in equation (8) instead of the nominal parameters extracted with the $e^+e^- \to p\bar{p}$ process.
- To estimate the uncertainty from the radiative corrections and vacuum polarization, we determine the product of the signal MC reconstruction efficiency $\varepsilon_{\mathrm{MC}}^i$ and the radiative correction factor $(1+\delta)^i$ for the final and previous form factor parameterization within the signal MC simulation. Additionally, we take into account the parameter uncertainty from the input model for the lineshape via sampling within the uncertainty band. The contributions are taken as the systematic uncertainty δ_{ISR}.
- Several category-specific systematic uncertainties are considered for non-universal selection criteria. δ_{T0} and δ_{MUC} are studied with a data-driven method similar to the efficiency correction studied in the previous section, while δ_{evt} and δ_{BDT} are studied by varying the requirements and comparing the outcomes to the nominal results.

For the systematic uncertainty on the Born cross section for one classification category $i=$ A, B and C, the contributions are added in quadrature to the following.

$$\delta\sigma_{\mathrm{B}}^i = \sqrt{\sum_k \delta_k^2}, (k = \mathrm{sel, fit, model, trg, T0}^{i=\mathrm{A}}, \mathrm{evt}^{i=\mathrm{B}}, \mathrm{BDT}^{i=\mathrm{B}}, \mathrm{MUC}^{i=\mathrm{B,C}}) \tag{11}$$

The systematic uncertainty $\delta\sigma_{\mathrm{B}}^i$ is propagated as shown in equation (3) to determine the corresponding uncertainty in the effective form factor $\delta|G^i|$. The individual systematic uncertainties $\delta\sigma_{\mathrm{B}}^i$ are combined with $\delta\sigma_{\mathrm{B}}^{\mathrm{comb}}$ and $\delta|G^{\mathrm{comb}}|$

using the generalized least-squares method[43] (equation (4)). The uncertainties δ_L and δ_{ISR} are considered only once with the expression for the systematic uncertainty $\delta\sigma_B$ and $\delta|G|$ in the final results.

$$\delta\sigma_B = \sqrt{(\delta\sigma_B^{comb})^2 + (\delta_L)^2 + (\delta_{ISR})^2}, \delta|G| = \sqrt{(\delta|G^{comb}|)^2 + (\delta_L)^2 + (\delta_{ISR})^2} \tag{12}$$

Data availability
Source data are provided with this paper. The raw data used for the plots within this paper and other findings of this study are archived in the Institute of High Energy Physics mass storage silo and are available from the corresponding author upon reasonable request.

Code availability
All algorithms used for data analysis and simulation are archived by the authors and are available on request.

References
34. Jegerlehner, F. Hadronic contributions to the photon vacuum polarization and their role in precision physics. *J. Phys. G* **29**, 101–110 (2003).
35. Ping, R. G. et al. Tuning and validation of hadronic event generator for *R* value measurements in the tau-charm region. *Chinese Phys. C* **40**, 113002 (2016).
36. Carloni Calame, C. M., Montagna, G., Nicrosini, O. & Piccinini, F. The BABAYAGA event generator. *Nucl. Phys. B Proc. Sup.* **131**, 48–55 (2004).
37. Ping, R. G. et al. Event generators at BESIII. *Chinese Phys. C* **32**, 599–602 (2008).
38. Ma, X. et al. Determination of event start time at BESIII. *Chinese Phys. C* **32**, 744–749 (2008).
39. James, F. MINUIT—function minimization and error analysis: reference manual version 94.1. *CERN-D506* (1994).
40. Fletcher, R. A new approach to variable metric algorithms. *Comput. J.* **13**, 317–322 (1970).
41. Ablikim, M. et al. Study of $J/\Psi \to p\bar{p}$ and $J/\Psi \to n\bar{p}$. *Phys. Rev. D* **86**, 032014 (2012).
42. Berger, N. et al. Trigger efficiencies at BESIII. *Chinese Phys. C* **34**, 1779–1784 (2010).
43. Schmelling, M. Averaging correlated data. *Phys. Scr.* **51**, 676–679 (1995).

Author contributions
All the authors have contributed to this publication, being variously involved in the design and construction of the detectors, writing software, calibrating sub-systems, operating the detectors, acquiring data and analysing the processed data.

Competing interests
The authors declare no competing interests.

Additional information
Supplementary information The online version contains supplementary material available at https://doi.org/10.1038/s41567-021-01345-6.

Peer review information *Nature Physics* thanks Hyun-Chul Kim, Galina Pakhlova and Bogdan Wojtsekhowski for their contribution to the peer review of this work.

Reprints and permissions information is available at www.nature.com/reprints.

The BESIII Collaboration

M. Ablikim[1], M. N. Achasov[2,77], P. Adlarson[3], S. Ahmed[4], M. Albrecht[5], R. Aliberti[6], A. Amoroso[7,8], Q. An[9,10], Anita Lavania[11], X. H. Bai[12], Y. Bai[13], O. Bakina[14], R. B. Ferroli[15], I. Balossino[16], Y. Ban[17,78], K. Begzsuren[5], N. Berger[6], M. Bertani[15], D. Bettoni[16], F. Bianchi[7,8], J. Biernat[3], J. Bloms[18], A. Bortone[7,8], I. Boyko[14], R. A. Briere[19], H. Cai[20], X. Cai[1,10], A. Calcaterra[15], G. F. Cao[1,21], N. Cao[1,21], S. A. Cetin[22], J. F. Chang[1,10], W. L. Chang[1,21], G. Chelkov[14,79], D. Y. Chen[23], G. Chen[1], H. S. Chen[1,21], M. L. Chen[1,10], S. J. Chen[24], X. R. Chen[25], Y. B. Chen[1,10], Z. J. Chen[26,80], W. S. Cheng[8], G. Cibinetto[16], F. Cossio[8], X. F. Cui[27], H. L. Dai[1,10], X. C. Dai[1,21], A. Dbeyssi[4], R. B. de Boer[5], D. Dedovich[14], Z. Y. Deng[1], A. Denig[6], I. Denysenko[14], M. Destefanis[7,8], F. De Mori[7,8], Y. Ding[28], C. Dong[27], J. Dong[1,10], L. Y. Dong[1,21], M. Y. Dong[1,10,21], X. Dong[20], S. X. Du[29], J. Fang[1,10], S. S. Fang[1,21], Y. Fang[1], R. Farinelli[16], L. Fava[8,30], F. Feldbauer[5], G. Felici[15], C. Q. Feng[9,10], M. Fritsch[5], C. D. Fu[1], Y. Fu[1], Ya Gao[31], Yang Gao[9,10], Yuanning Gao[17,78], Y. G. Gao[23], I. Garzia[16,32], E. M. Gersabeck[33], A. Gilman[34], K. Goetzen[35], L. Gong[27], W. X. Gong[1,10], W. Gradl[6], M. Greco[7,8], L. M. Gu[24], M. H. Gu[1,10], S. Gu[36], Y. T. Gu[37], C. Y. Guan[1,21], A. Q. Guo[38], L. B. Guo[39], R. P. Guo[40], Y. P. Guo[41,81], A. Guskov[14], T. T. Han[42], X. Q. Hao[43], F. A. Harris[44], K. L. He[1,21], F. H. Heinsius[5], C. H. Heinz[6], T. Held[5], Y. K. Heng[1,10,21], C. Herold[45], M. Himmelreich[35,82], T. Holtmann[5], Y. R. Hou[21], Z. L. Hou[1], H. M. Hu[1,21], J. F. Hu[46,83], T. Hu[1,10,21], Y. Hu[1], G. S. Huang[9,10], L. Q. Huang[31], X. T. Huang[42], Y. P. Huang[1], Z. Huang[17,78], N. Huesken[18], T. Hussain[47], W. I. Andersson[3], W. Imoehl[38], M. Irshad[9,10], S. Jaeger[5], S. Janchiv[84], Q. Ji[1], Q. P. Ji[43], X. B. Ji[1,21], X. L. Ji[1,10], H. B. Jiang[42], X. S. Jiang[1,10,21], X. Y. Jiang[27], J. B. Jiao[42], Z. Jiao[48], S. Jin[24], Y. Jin[12], T. Johansson[3], N. Kalantar-Nayestanaki[49], X. S. Kang[28], R. Kappert[49], M. Kavatsyuk[49], B. C. Ke[1,50], I. K. Keshk[5], A. Khoukaz[18], P. Kiese[6], R. Kiuchi[1], R. Kliemt[35], L. Koch[51], O. B. Kolcu[22,85], B. Kopf[5], M. Kuemmel[5], M. Kuessner[5], A. Kupsc[3], M. G. Kurth[1,21], W. Kühn[51], J. J. Lane[33], J. S. Lange[51], P. Larin[4], L. Lavezzi[7,8], Z. H. Lei[9,10], H. Leithoff[6], M. Lellmann[6], T. Lenz[6], C. Li[52], C. H. Li[53], Cheng Li[9,10], D. M. Li[29], F. Li[1,10], G. Li[1], H. Li[9,10], H. Li[50], H. B. Li[1,21], H. J. Li[41,81], H. N. Li[46,83], J. L. Li[42], J. Q. Li[5], Ke Li[1], L. K. Li[1], Lei Li[54], P. L. Li[9,10], P. R. Li[55], S. Y. Li[56], W. D. Li[1,21], W. G. Li[1], X. H. Li[9,10], X. L. Li[42], Z. Y. Li[57], H. Liang[9,10], H. Liang[1,21], Y. F. Liang[58], Y. T. Liang[25], L. Z. Liao[1,21], J. Libby[11], C. X. Lin[57], B. J. Liu[1], C. X. Liu[1], D. Liu[9,10], F. H. Liu[59], Fang Liu[1], Feng Liu[23], H. B. Liu[37], H. M. Liu[1,21], Huanhuan Liu[1], Huihui Liu[60], J. B. Liu[9,10], J. Y. Liu[1,21], K. Liu[1], K. Y. Liu[28], Ke Liu[23], L. Liu[9,10], M. H. Liu[41,81], Q. Liu[21], S. B. Liu[9,10], S. Liu[61], T. Liu[1,21], W. M. Liu[9,10], X. Liu[55], Y. B. Liu[27], Z. A. Liu[1,10,21], Z. Q. Liu[42], X. C. Lou[1,10,21], F. X. Lu[43], H. J. Lu[48], J. D. Lu[1,21], J. G. Lu[1,10], X. L. Lu[1], Y. Lu[1], Y. P. Lu[1,10], C. L. Luo[39], M. X. Luo[62], P. W. Luo[57], T. Luo[41,81], X. L. Luo[1,10], S. Lusso[8], X. R. Lyu[21], F. C. Ma[28], H. L. Ma[1], L. L. Ma[42], M. M. Ma[1,21], Q. M. Ma[1], R. Q. Ma[1,21], R. T. Ma[21], X. N. Ma[27], X. X. Ma[1,21], X. Y. Ma[1,10], F. E. Maas[4], M. Maggiora[7,8], S. Maldaner[6], S. Malde[63], Q. A. Malik[47], A. Mangoni[64], Y. J. Mao[17,78], Z. P. Mao[1], S. Marcello[7,8], Z. X. Meng[12], J. G. Messchendorp[49], G. Mezzadri[16], T. J. Min[24], R. E. Mitchell[38], X. H. Mo[1,10,21], Y. J. Mo[23], N. Y. Muchnoi[2,77], H. Muramatsu[34], S. Nakhoul[35,82], Y. Nefedov[14], F. Nerling[35,82], I. B. Nikolaev[2,77], Z. Ning[1,10], S. Nisar[65,86], S. L. Olsen[21], Q. Ouyang[1,10,21], S. Pacetti[64,66], X. Pan[41,81], Y. Pan[33], A. Pathak[1], P. Patteri[15], M. Pelizaeus[5], H. P. Peng[9,10], K. Peters[35,82], J. Pettersson[3], J. L. Ping[39], R. G. Ping[1,21], A. Pitka[5], R. Poling[34], V. Prasad[9,10], H. Qi[9,10], H. R. Qi[56], K. H. Qi[25], M. Qi[24], T. Y. Qi[36], T. Y. Qi[41], S. Qian[1,10], W.-B. Qian[21], Z. Qian[57], C. F. Qiao[21], L. Q. Qin[67], X. S. Qin[5], Z. H. Qin[1,10], J. F. Qiu[1], S. Q. Qu[27], K. H. Rashid[47], K. Ravindran[11], C. F. Redmer[6], A. Rivetti[8], V. Rodin[49], M. Rolo[8], G. Rong[1,21], Ch. Rosner[4], M. Rump[18], H. S. Sang[9], A. Sarantsev[14,87], Y. Schelhaas[6], C. Schnier[5], K. Schoenning[3], M. Scodeggio[16], D. C. Shan[61], W. Shan[68], X. Y. Shan[9,10], M. Shao[9,10], C. P. Shen[41], P. X. Shen[27], X. Y. Shen[1,21], H. C. Shi[9,10], R. S. Shi[1,21], X. Shi[1,10], X. D. Shi[9,10], W. M. Song[1,69], Y. X. Song[17,78],

S. Sosio[7,8], **S. Spataro**[7,8], **K. X. Su**[20], **F. F. Sui**[42], **G. X. Sun**[1], **H. K. Sun**[1], **J. F. Sun**[43], **L. Sun**[20], **S. S. Sun**[1,21], **T. Sun**[1,21], **W. Y. Sun**[39], **X. Sun**[26,80], **Y. J. Sun**[9,10], **Y. K. Sun**[9,10], **Y. Z. Sun**[1], **Z. T. Sun**[1], **Y. H. Tan**[20], **Y. X. Tan**[9,10], **C. J. Tang**[58], **G. Y. Tang**[1], **J. Tang**[57], **J. X. Teng**[9,10], **V. Thoren**[3], **I. Uman**[70], **B. Wang**[1], **C. W. Wang**[24], **D. Y. Wang**[17,78], **H. P. Wang**[1,21], **K. Wang**[1,10], **L. L. Wang**[1], **Meng Wang**[1,21,42], **M. Z. Wang**[17,78], **W. H. Wang**[20], **W. P. Wang**[9,10], **X. Wang**[17,78], **X. F. Wang**[55], **X. L. Wang**[41,81], **Yue Wang**[9,10], **Ying Wang**[57], **Y. D. Wang**[71], **Y. F. Wang**[1,10,21], **Y. Q. Wang**[1], **Z. Wang**[1,10], **Z. Y. Wang**[1], **Z. Wang**[21], **D. H. Wei**[67], **P. Weidenkaff**[6], **F. Weidner**[18], **S. P. Wen**[1], **D. J. White**[33], **U. Wiedner**[5], **G. Wilkinson**[63], **M. Wolke**[3], **L. Wollenberg**[5], **J. F. Wu**[1,21], **L. H. Wu**[1], **L. J. Wu**[1,21], **X. Wu**[41,81], **Z. Wu**[1,10], **L. Xia**[9,10], **H. Xiao**[41,81], **S. Y. Xiao**[1], **Y. J. Xiao**[1,21], **Z. J. Xiao**[39], **X. H. Xie**[17,78], **Y. G. Xie**[1,10], **Y. H. Xie**[23], **T. Y. Xing**[1,21], **G. F. Xu**[1], **J. J. Xu**[24], **Q. J. Xu**[72], **W. Xu**[1,21], **X. P. Xu**[61], **F. Yan**[41,81], **L. Yan**[41,81], **W. B. Yan**[9,10], **W. C. Yan**[29], **X. Yan**[61], **H. J. Yang**[73,88], **H. X. Yang**[1], **L. Yang**[50], **R. X. Yang**[9,10], **S. L. Yang**[21], **Y. H. Yang**[24], **Y. X. Yang**[67], **Y. Yang**[1,21], **Z. Yang**[25], **M. Ye**[1,10], **M. H. Ye**[74], **J. H. Yin**[1], **Z. Y. You**[57], **B. X. Yu**[1,10,21], **C. X. Yu**[27], **G. Yu**[1,21], **J. S. Yu**[26,80], **T. Yu**[31], **C. Z. Yuan**[1,21], **L. Yuan**[36], **W. Yuan**[7,8], **X. Q. Yuan**[17,78], **Y. Yuan**[1], **Z. Y. Yuan**[57], **C. X. Yue**[53], **A. Yuncu**[22,89], **A. A. Zafar**[47], **Y. Zeng**[26,80], **B. X. Zhang**[1], **G. Zhang**[43], **H. Zhang**[9], **H. H. Zhang**[57], **H. Y. Zhang**[1,10], **J. J. Zhang**[50], **J. L. Zhang**[75], **J. Q. Zhang**[5], **J. W. Zhang**[1,10,21,84], **Y. Zhang**[1], **J. Z. Zhang**[1,21], **Jianyu Zhang**[1,21], **Jiawei Zhang**[1,21], **L. Zhang**[1], **Lei Zhang**[24], **S. Zhang**[57], **S. F. Zhang**[24], **X. D. Zhang**[71], **X. Y. Zhang**[42], **Y. Zhang**[63], **Y. H. Zhang**[1,10], **Y. T. Zhang**[9,10], **Yan Zhang**[9,10], **Yao Zhang**[1], **Yi Zhang**[41,81], **Z. H. Zhang**[23], **Z. Y. Zhang**[20], **G. Zhao**[1], **J. Zhao**[53], **J. Y. Zhao**[1,21], **J. Z. Zhao**[1,10], **Lei Zhao**[9,10], **Ling Zhao**[1], **M. G. Zhao**[27], **Q. Zhao**[1], **S. J. Zhao**[29], **Y. B. Zhao**[1,10], **Y. X. Zhao**[25], **Z. G. Zhao**[9,10], **A. Zhemchugov**[14,79], **B. Zheng**[31], **J. P. Zheng**[1,10], **Y. Zheng**[17,78], **Y. H. Zheng**[21], **B. Zhong**[39], **C. Zhong**[31], **L. P. Zhou**[1,21], **Q. Zhou**[1,21], **X. Zhou**[20], **X. K. Zhou**[21], **X. R. Zhou**[9,10], **A. N. Zhu**[1,21], **J. Zhu**[27], **K. Zhu**[1], **K. J. Zhu**[1,10,21], **S. H. Zhu**[76], **W. J. Zhu**[27], **X. L. Zhu**[56], **Y. C. Zhu**[9,10], **Z. A. Zhu**[1,21], **B. S. Zou**[1] and **J. H. Zou**[1]

[1]Institute of High Energy Physics, Beijing, People's Republic of China. [2]G.I. Budker Institute of Nuclear Physics (BINP) SB RAS, Novosibirsk, Russia. [3]Uppsala University, Uppsala, Sweden. [4]Helmholtz Institute Mainz, Mainz, Germany. [5]Ruhr-University Bochum, Bochum, Germany. [6]Johannes Gutenberg University of Mainz, Mainz, Germany. [7]University of Turin, Turin, Italy. [8]INFN, Turin, Italy. [9]University of Science and Technology of China, Hefei, People's Republic of China. [10]State Key Laboratory of Particle Detection and Electronics, Beijing, People's Republic of China. [11]Indian Institute of Technology Madras, Chennai, India. [12]University of Jinan, Jinan, People's Republic of China. [13]Southeast University, Nanjing, People's Republic of China. [14]Joint Institute for Nuclear Research, Dubna, Russia. [15]INFN Laboratori Nazionali di Frascati, Frascati, Italy. [16]INFN Sezione di Ferrara, Ferrara, Italy. [17]Peking University, Beijing, People's Republic of China. [18]University of Muenster, Muenster, Germany. [19]Carnegie Mellon University, Pittsburgh, PA, USA. [20]Wuhan University, Wuhan, People's Republic of China. [21]University of Chinese Academy of Sciences, Beijing, People's Republic of China. [22]Istanbul Bilgi University, Istanbul, Turkey. [23]Central China Normal University, Wuhan, People's Republic of China. [24]Nanjing University, Nanjing, People's Republic of China. [25]Institute of Modern Physics, Lanzhou, People's Republic of China. [26]Hunan University, Changsha, People's Republic of China. [27]Nankai University, Tianjin, People's Republic of China. [28]Liaoning University, Shenyang, People's Republic of China. [29]Zhengzhou University, Zhengzhou, People's Republic of China. [30]University of Eastern Piedmont, Alessandria, Italy. [31]University of South China, Hengyang, People's Republic of China. [32]University of Ferrara, Ferrara, Italy. [33]University of Manchester, Manchester, United Kingdom. [34]University of Minnesota, Minneapolis, MN, USA. [35]GSI Helmholtz Centre for Heavy Ion Research, Darmstadt, Germany. [36]Beihang University, Beijing, People's Republic of China. [37]Guangxi University, Nanning, People's Republic of China. [38]Indiana University, Bloomington, IN, USA. [39]Nanjing Normal University, Nanjing, People's Republic of China. [40]Shandong Normal University, Jinan, People's Republic of China. [41]Fudan University, Shanghai, People's Republic of China. [42]Shandong University, Jinan, People's Republic of China. [43]Henan Normal University, Xinxiang, People's Republic of China. [44]University of Hawaii, Honolulu, HI, USA. [45]Suranaree University of Technology, Nakhon Ratchasima, Thailand. [46]South China Normal University, Guangzhou, People's Republic of China. [47]University of the Punjab, Lahore, Pakistan. [48]Huangshan College, Huangshan, People's Republic of China. [49]KVI-CART, University of Groningen, Groningen, The Netherlands. [50]Shanxi Normal University, Linfen, People's Republic of China. [51]Justus-Liebig-Universität Giessen, II. Physikalisches Institut, Giessen, Germany. [52]Qufu Normal University, Qufu, People's Republic of China. [53]Liaoning Normal University, Dalian, People's Republic of China. [54]Beijing Institute of Petrochemical Technology, Beijing, People's Republic of China. [55]Lanzhou University, Lanzhou, People's Republic of China. [56]Tsinghua University, Beijing, People's Republic of China. [57]Sun Yat-Sen University, Guangzhou, People's Republic of China. [58]Sichuan University, Chengdu, People's Republic of China. [59]Shanxi University, Taiyuan, People's Republic of China. [60]Henan University of Science and Technology, Luoyang, People's Republic of China. [61]Soochow University, Suzhou, People's Republic of China. [62]Zhejiang University, Hangzhou, People's Republic of China. [63]University of Oxford, Oxford, UK. [64]INFN Sezione di Perugia, Perugia, Italy. [65]COMSATS University Islamabad, Lahore, Pakistan. [66]University of Perugia, Perugia, Italy. [67]Guangxi Normal University, Guilin, People's Republic of China. [68]Hunan Normal University, Changsha, People's Republic of China. [69]Jilin University, Changchun, People's Republic of China. [70]Near East University, Nicosia, North Cyprus, Mersin, Turkey. [71]North China Electric Power University, Beijing, People's Republic of China. [72]Hangzhou Normal University, Hangzhou, People's Republic of China. [73]Shanghai Jiao Tong University, Shanghai, People's Republic of China. [74]China Center of Advanced Science and Technology, Beijing, People's Republic of China. [75]Xinyang Normal University, Xinyang, People's Republic of China. [76]University of Science and Technology Liaoning, Anshan, People's Republic of China. [77]Present address: The Novosibirsk State University, Novosibirsk, Russia. [78]Present address: State Key Laboratory of Nuclear Physics and Technology, Peking University, Beijing, People's Republic of China. [79]Present address: The Moscow Institute of Physics and Technology, Moscow, Russia. [80]Present address:

School of Physics and Electronics, Hunan University, Changsha, China. [81]Present address: Key Laboratory of Nuclear Physics and Ion-beam Application (MOE) and Institute of Modern Physics, Fudan University, Shanghai, People's Republic of China. [82]Present address: Goethe University Frankfurt, Frankfurt am Main, Germany. [83]Present address: Guangdong Provincial Key Laboratory of Nuclear Science, Institute of Quantum Matter, South China Normal University, Guangzhou, China. [84]Present address: Institute of Physics and Technology, Ulaanbaatar, Mongolia. [85]Present address: Istanbul Arel University, Istanbul, Turkey. [86]Present address: Department of Physics, Harvard University, Cambridge, MA, USA. [87]Present address: The NRC 'Kurchatov Institute', PNPI, Gatchina, Russia. [88]Present address: Key Laboratory for Particle Physics, Astrophysics and Cosmology, Ministry of Education; Shanghai Key Laboratory for Particle Physics and Cosmology, Institute of Nuclear and Particle Physics, Shanghai, People's Republic of China. [89]Present address: Bogazici University, Istanbul, Turkey.